Hindawi
International Journal of Photoenergy
Volume 2020, Article ID 4539472, 9 pages
https://doi.org/10.1155/2020/4539472

Research Article

Synthesis of TiO_2/Pd and TiO_2/PdO Hollow Spheres and Their Visible Light Photocatalytic Activity

Jing Yan, Xiaojuan Li, Bo Jin, Min Zeng, and Rufang Peng

State Key Laboratory Cultivation Base for Nonmetal Composites and Functional Materials, Southwest University of Science and Technology, Mianyang 621010, China

Correspondence should be addressed to Bo Jin; jinbo0428@163.com

Received 26 December 2019; Accepted 24 February 2020; Published 15 April 2020

Academic Editor: Zaiyong Jiang

A series of TiO_2, TiO_2/Pd, and TiO_2/PdO hollow sphere photocatalysts was successfully prepared *via* a combination of hydrothermal, sol-immobilization, and calcination methods. The structure and optical properties of the as-prepared samples were characterized by X-ray diffraction, field emission scanning electron microscopy, transmission electron microscopy, Brunauer-Emmett-Telleranalysis, Barrett-Joyner-Halenda measurement, and UV-Vis diffuse reflectance spectroscopy. The photocatalysis efficiencies of all samples were evaluated through the photocatalytic degradation of rhodamine B under visible light irradiation. Results indicated that TiO_2/PdO demonstrated a higher photocatalytic activity (the photocatalytic degradation efficiency could reach up to 100% within 40 min) than the other samples and could maintain a stable photocatalytic degradation efficiency for at least four cycles. Finally, after using different scavengers, superoxide and hydroxyl radicals were identified as the primary active species for the effectiveness of the TiO_2/PdO photocatalyst.

1. Introduction

Semiconductor materials have been received and extensively applied as photocatalysts in photocatalytic water splitting and photodegradation of organic pollutants. TiO_2 is an important semiconductor in wide applications, such as in photocatalysts [1, 2], solar cells [3], electrorheology [4, 5], and antibacterial agents [6]. It has been exhaustively explored for its merits of environment friendliness, chemical inertness, high stability, nontoxicity, and low cost when utilized as a photocatalyst for environment remediation and photodegradation of organic pollutants [7–9].

Xiang et al. [10] successfully synthesized 3D urchin-like TiO_2 microspheres for photocatalytic applications. Lai et al. [11] prepared hierarchical TiO_2 and hierarchical nanosheet-assembled yolk-shell TiO_2 microspheres for dye adsorption and photocatalysis, respectively. Sarkar and Chattopadhyay [12] synthesized a large-scale mesoporous TiO_2 microsphere for photocatalysis degradation. However, these TiO_2 photocatalysts exhibit high photocatalytic activity only under UV irradiation. This finding can be ascribed to the intrinsic properties of TiO_2: a wide band gap (3.2 eV), which limits its use in the UV region of the solar spectrum, which accounts for a very small fraction of solar energy [13]. Therefore significant efforts have been devoted to modify the band gap of TiO_2. Doping to extend the optical absorption of TiO_2 into the visible spectrum is an effective method. In recent decades, doping with metals or nonmetals has been performed to shift the optical response of the catalytically active TiO_2 from the UV to the visible light region. For example, mordenite [14], graphene [15, 16], F [17], Sm [18], Ni [19], Pt [20], Au [21], Ag [22], and Pd [23, 24] have been used to extend the photoresponse range of TiO_2. Similar to Pd, doped PdO can form a certain number of heterojunctions with TiO_2, thereby inhibiting the recombination of photogenerated carriers, improving the light utilization efficiency and catalytic activity.

In this study, we successfully synthesized TiO_2/Pd and TiO_2/PdO hollow sphere photocatalysts following the methods of Li et al. [25]. The methods combined hydrothermal, sol-immobilization, and calcination. We selected rhodamine B (Rh B) as the dye template for studying the

photocatalytic degradation efficiency of the as-prepared samples under visible light [26]. The results exhibited that TiO_2/PdO demonstrated a higher photocatalytic activity than previously reported photocatalysts [27, 28] because TiO_2/PdO possessed a wide range of optical absorption, high crystallinity, and a large pore size. Moreover, the photocatalytic reaction mechanism was also discussed on the basis of trapping experiments of active species.

2. Experimental Section

2.1. Materials. Titanium butoxide (TBOT), palladium chloride ($PdCl_2$), and rhodamine B (Rh B) were purchased from Aladdin Regent Company. Absolute ethanol, N, N-dimethylformamide (DMF), trifluoroacetic acid (TFA), P-benzoquinone (BQ), isopropanol (IPA), and potassium iodide (KI) were obtained from Kelong Chemical Reagent Company.

2.2. Synthesis of TiO_2 Hollow Spheres. We followed the methods of Li et al. to prepare the TiO_2 hollow spheres [25]. In a typical procedure, a homogeneous solution including 51 mL of H_2O, 14.1 mL of DMF, and 6.9 mL of TFA was dropped to 2.04 mL of TBOT in a Teflon-lined autoclave, and then the mixture solution was heated to 180°C and maintained this temperature for 24 h. After cooling to room temperature, the white precipitate was obtained and washed with absolute ethanol and distilled water three times, respectively. Then, the obtained TiO_2 hollow spheres were dried in a vacuum at 60°C and calcined at 450°C for 3 h in air. The TiO_2 hollow spheres before and after calcination were denoted TiO_2 and TiO_2-T, respectively.

2.3. Synthesis of TiO_2/Pd and TiO_2/PdO Hollow Spheres. Pd nanoparticles were supported on TiO_2 hollow spheres by using the methods of Li et al. [25]. An aqueous solution of $PdCl_2$ (10 mL) and polyvinyl alcohol (PVA, 1 wt%, 0.72 mL) were diluted with water (120 mL). After stirring for 30 min, 1.98 mL $NaBH_4$ solution (0.1 M) was added to form a dark brown solution. Subsequently, sulfuric acid solution was added to adjust the pH to 1. Then, 0.2 g TiO_2 was ultrasonically dispersed in this mixture and rapidly stirred for 2 hours. The resulting slurry was filtered, washed with absolute alcohol, and distilled water, respectively. The obtained TiO_2/Pd hollow spheres were dried in a vacuum at 60°C and calcined at 450°C for 3 h in air. The TiO_2/Pd hollow spheres before and after calcination were denoted TiO_2/Pd and TiO_2/PdO, respectively.

2.4. Characterization. X-ray diffraction (XRD, Philips X'Pert PRO, Netherlands) on a diffractometer equipped with Cu Kα radiation ($k = 0.15418$ nm) from 20° to 80° at a scanning speed of 2° min^{-1}. The morphology and detailed structural information of the samples were observed using a field emission scanning electron microscope (FESEM, Ultra 55, CARL ZEISS in Germany) and transmission electron microscopy (TEM, Libra 200 PE, operated at 200 kV, Germany). The nitrogen adsorption-desorption isotherms were measured at 77 K using a Micromeritics ASAP 2000 system, and the surface area and pore size distribution were calculated using the Brunauer-Emmett-Teller (BET) and Barrett-Joyner-Halenda (BJH) methods, respectively. The optical spectra were examined by using a Hitachi U-4100 UV-Vis diffuse reflectance spectra (UV-Vis DRS) in the wavelength range of 200-800 nm equipped with the integrating sphere accessory for diffuse reflectance spectra.

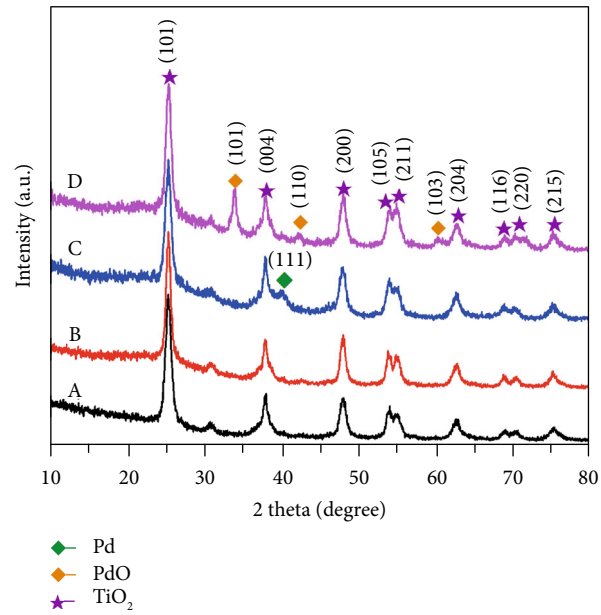

FIGURE 1: Typical XRD patterns of (a)TiO_2, (b)TiO_2-T, (c)TiO_2/Pd, and (d)TiO_2/PdO.

2.5. Photocatalytic Activity Measurement. Photocatalytic activities of the as-synthesized products were studied using Rh B as a model pollutant under visible light irradiation. The photocatalytic reactor (Beijing NBT Technology Co., Ltd.) consisted of quartz glass with a circulating water jack and a light source (A 500 W xenon lamp). There is circulating water between the reaction system and the xenon lamp to remove the thermal effect of light. The experiments were performed at room temperature. For each photocatalytic activity measurement, 30 mg of photocatalyst was added to 50 mL of Rh B aqueous solution with the concentration of 30 mg/L. Before irradiation, the reaction mixture was stirred in the dark at 25°C for 20 min to ensure the establishment of absorption/desorption equilibrium between the photocatalysts and Rh B solution. After the absorption equilibrium, the suspension solution was irradiated by the visible light with continuous stirring. At the given intervals, 5 mL of reaction mixture was centrifuged and then analyzed by recording variations of the maximum absorption spectra by UV1600 spectrometer [29].

3. Results and Discussion

3.1. X-Ray Diffraction (XRD) Analysis. Figure 1 shows the typical XRD patterns of TiO_2, TiO_2-T, TiO_2/Pd, and TiO_2/PdO. The main diffraction peaks at $2\theta = 25.3°$, 37.9°, 48.1°, 53.8°, 55.0°, 62.7°, 68.8°, 70.2°, and 75.1° in the spectrum of TiO_2 and the composite samples were identified and attributed to the diffraction faces of (101), (004), (200),

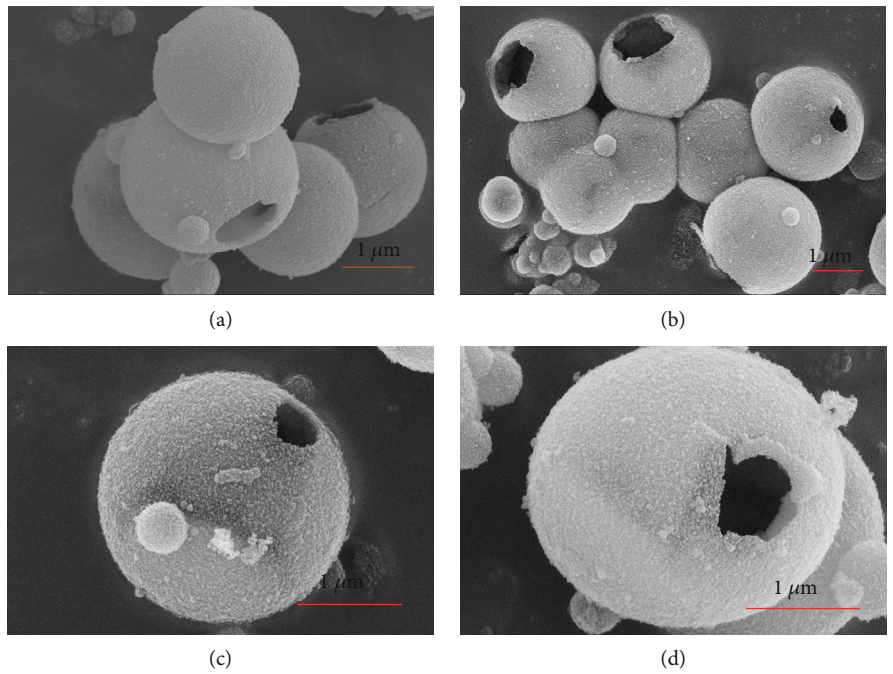

Figure 2: FESEM images of (a)TiO_2, (b)TiO_2-T, (c)TiO_2/Pd, and (d)TiO_2/PdO.

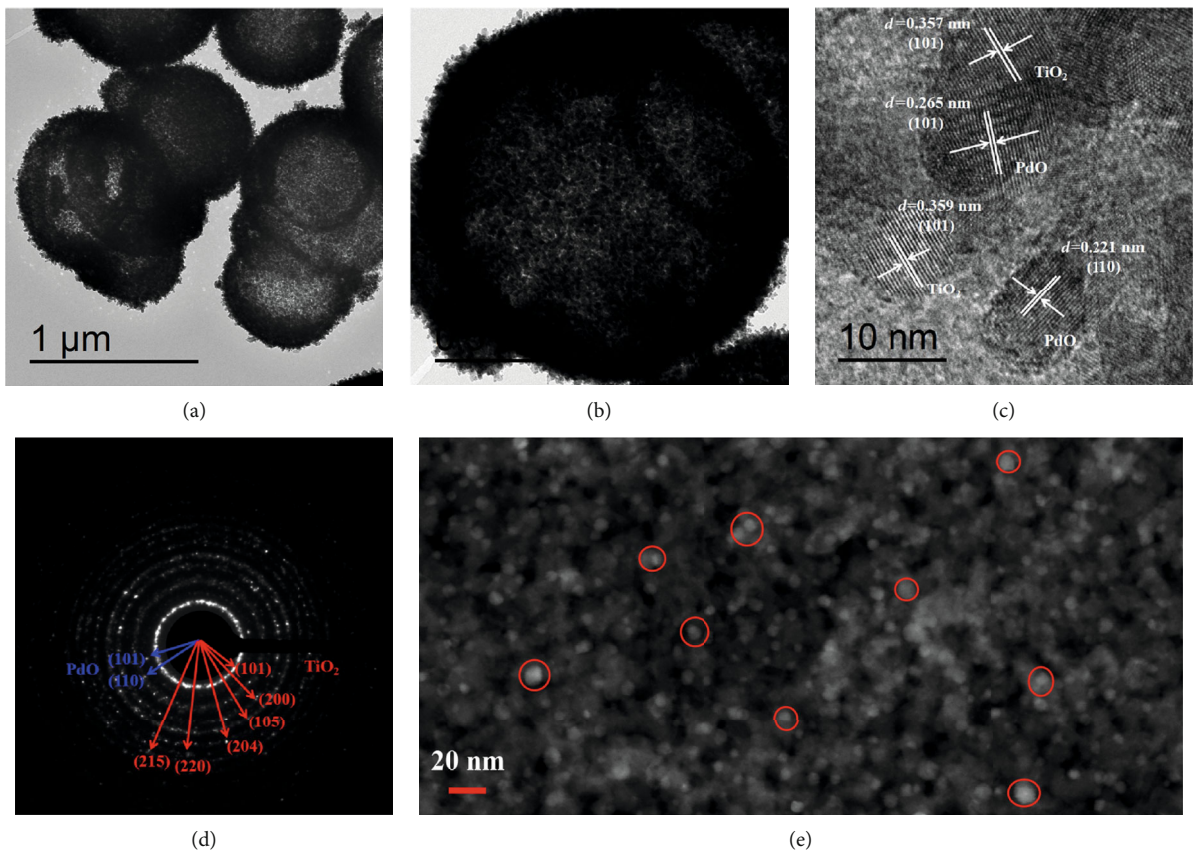

Figure 3: TEM (a, b), HRTEM (c), SAED (d), and STEM (e) images of TiO_2/PdO.

(105), (211), (204), (116), (220), and (215), respectively, showing the crystal phase of anatase (JCPDS no. 21-1272) and implying that calcination and the doping of Pd (the diffraction peak at $2\theta = 40.1^\circ$, JCPDS no. 87-0639) and PdO (the diffraction peaks at $2\theta = 33.8^\circ$, 42.2°, and 60.2°, JCPDS no. 43-1024) did not change the structure of TiO_2. These

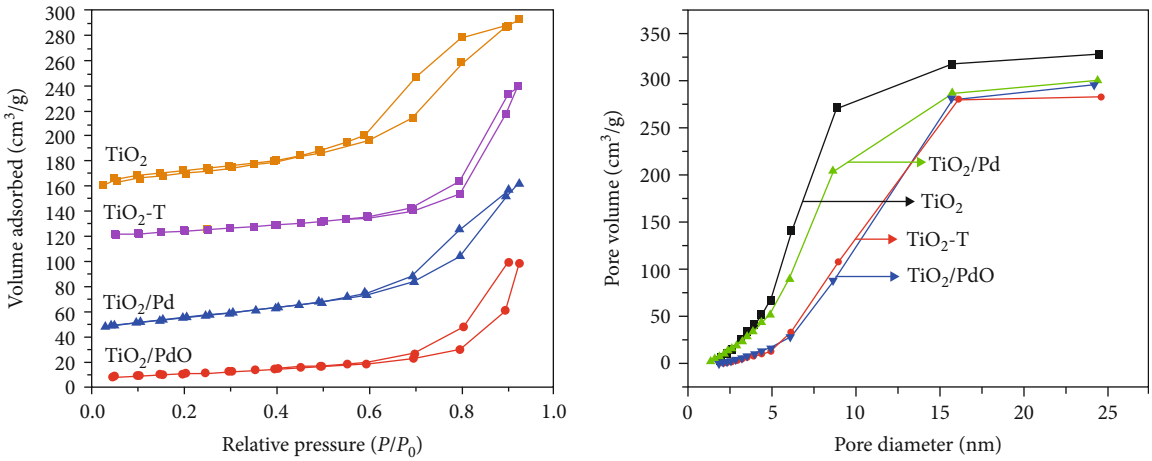

Figure 4: (a) N_2 adsorption-desorption isotherms and (b) pore size distribution of TiO_2, TiO_2-T, TiO_2/Pd, and TiO_2/PdO.

Table 1: Microstructure of TiO_2, TiO_2-T, TiO_2/Pd, and TiO_2/PdO.

Samples	TiO_2	TiO_2-T	TiO_2/Pd	TiO_2/PdO
S_{BET} (m^2/g)	112.316	63.919	96.796	65.506
Average pore size (nm)	9.9017	15.8853	10.7378	16.5032

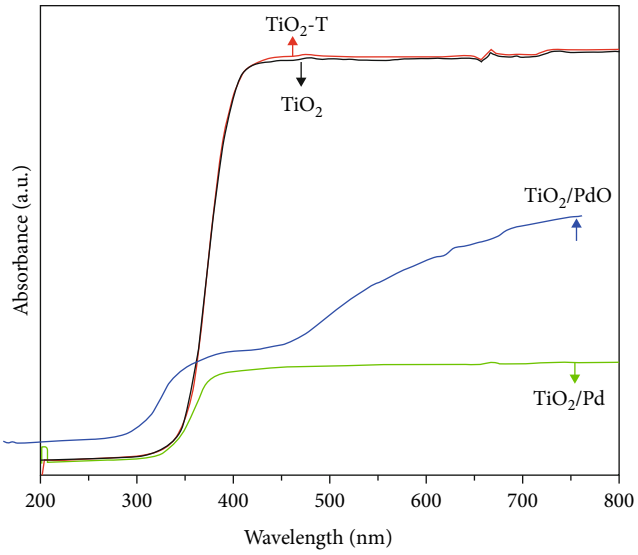

Figure 5: UV-Vis diffusive reflectance spectra of TiO_2, TiO_2-T, TiO_2/Pd, and TiO_2/PdO.

results show that the diffraction peaks of TiO_2-T and TiO_2/PdO were stronger and narrower than those of TiO_2 and TiO_2/Pd, indicating that the crystallinity of TiO_2-T and TiO_2/PdO improved through calcination.

3.2. Scanning Electron Microscopy (SEM) Analysis. The morphology of TiO_2, TiO_2-T, TiO_2/Pd, and TiO_2/PdO was characterized by SEM and is shown in Figure 2. The result implies that samples with an average diameter of approximately 2-3 μm were successfully synthesized. The hollow spheres obtained exhibited thin and coarse shells with a large cavity space, which can be observed from the fragment. Most of the hollow sphere shells had holes, which may be caused by the collision during the hydrothermal reaction or the centrifugation step [30].

Table 2: Photoabsorption edge and band gap energy of TiO_2, TiO_2-T, TiO_2/Pd, and TiO_2/PdO.

Samples	Absorption edge (nm)	Band gap (eV)
TiO_2	380	3.26
TiO_2-T	397	3.12
TiO_2/Pd	406	3.05
TiO_2/PdO	503	2.47

3.3. Transmission Electron Microscopy (TEM) Analysis. The morphology and crystal structure of TiO_2/PdO were examined by TEM, as shown in Figure 3. Figures 3(a) and 3(b) are different magnification TEM images showing that TiO_2/PdO has hollow structures, which is consistent with the results of SEM. TiO_2/PdO displayed clear lattice fringes, suggesting its crystalline nature as shown in Figure 3(c). The lattice fringes were measured to be 0.357 and 0.221 nm, which correspond to the (101) and (110) planes of TiO_2 (JCPDS no. 21-1272) and PdO (JCPDS no. 43-1024), respectively. Further analysis of the crystal structure was performed by selected area electron diffraction (SAED) pattern as shown in Figure 3(d). The rings of the SAED patterns can be indexed to the crystalline phases of PdO and TiO_2. The SAED results indicate the presence of the (101) and (110) planes for crystalline PdO as derived from the lighter ring and the (101), (200), (105), (204), (220), and (215) planes from the brighter ring for crystalline TiO_2. The planes obtained from the HRTEM and SAED pattern for both PdO and TiO_2 matched the XRD results well. The STEM image of TiO_2/PdO is shown in Figure 3(e). The white spots in the STEM image are the homogenous dispersion of PdO particles on the TiO_2 [31, 32].

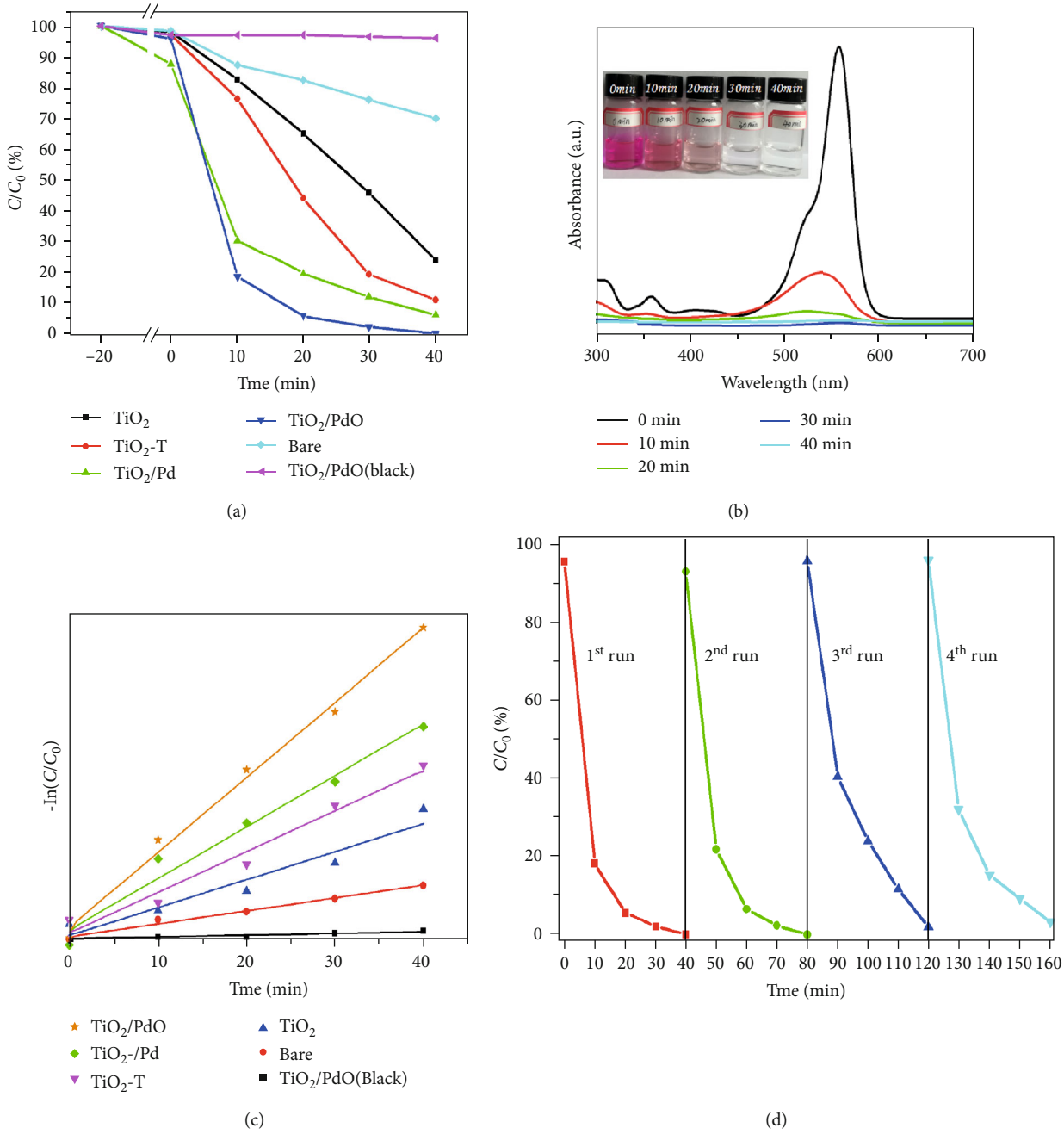

FIGURE 6: (a) Photocatalytic degradation of Rh B solution with TiO_2, TiO_2-T, TiO_2/Pd, and TiO_2/PdO under visible light irradiation. (b) UV-Vis absorption spectra of Rh B in the presence of TiO_2/PdO at different photocatalytic degradation times. (c) Kinetics of Rh B photocatalytic degradation over TiO_2, TiO_2-T, TiO_2/Pd, and TiO_2/PdO under visible light irradiation. (d) Recycling of TiO_2/PdO for photocatalytic degradation of Rh B.

3.4. Brunauer-Emmett-Teller (BET) and Barrett-Joyner-Halenda (BJH) Analyses. Figure 4 presents the nitrogen adsorption-desorption isotherms and pore size distribution curve of TiO_2, TiO_2-T, TiO_2/Pd, and TiO_2/PdO. The isotherms of these samples could be attributed to type IV, and the curves exhibited hysteresis loops at high relative pressures, indicating a mesoporous structure. Furthermore, the specific surface areas and average pore sizes of these samples are summarized in Table 1. As calculated by the BET method, TiO_2-T and TiO_2/PdO resulted in BET surface areas of 63.919 and 65.506 m^2/g and relatively large average pore sizes of 15.8853 and 16.5032 nm, respectively. However, the BET surface areas of TiO_2-T and TiO_2/PdO were smaller than those of TiO_2 (112.316 m^2/g) and TiO_2/Pd (96.796 m^2/g), and the average pore sizes of TiO_2-T and TiO_2/PdO were larger than those of TiO_2 (9.9017 nm) and TiO_2/Pd (10.7378 nm). This result may be because the average pore size is related to the crystallite size of a sample [33]. When the hollow spheres were calcining, the crystallites located in the inner cores were easier to dissolve than the exterior

nanoparticles, the exterior nanoparticles could serve as the new starting site for the subsequent recrystallization process, and continued crystal growth could lead to the increased crystallite size of the sample [30]. Therefore, the average pore sizes of TiO_2-T and TiO_2/PdO after calcinations were larger than those of TiO_2 and TiO_2/Pd without calcination. The specific surface area of the catalyst is mainly determined by the pore wall area in the crystal. Due to the high-temperature calcination process, the hollow spheres dissolved and grew, which would cause the pores in the crystal to collapse and lose fine voids. Therefore, the BET specific surface areas of the calcined TiO_2-T and TiO_2/PdO were smaller than that of the uncalcined TiO_2 and TiO_2/PdO [34].

3.5. UV-Vis Diffusive Reflectance Spectra (UV-Vis DRS) Analysis. Figure 5 shows the UV-Vis adsorption spectra of TiO_2, TiO_2-T, TiO_2/Pd, and TiO_2/PdO. The corresponding absorption edge wavelengths and band gaps are summarized in Table 2. The band gap energy can be estimated by using the equation $E_g = 1240/\lambda_g$, where E_g is the band gap energy (eV) and λ_g is the wavelength (nm) of the absorption edge in the spectrum, respectively. The absorption spectra of TiO_2 and TiO_2-T were only in the ultraviolet region and can be ascribed to the intrinsic band gap absorption of TiO_2. Compared with those of TiO_2 and TiO_2-T, the absorption spectra of TiO_2/Pd and TiO_2/PdO showed more absorption in the visible range (400-700 nm). The absorption intensities in the visible light region decreased in the order of TiO_2/PdO>TiO_2/Pd>TiO_2-T>TiO_2. In other words, the band gap energies decreased in the order of TiO_2>TiO_2-T>TiO_2/Pd>TiO_2/PdO. Numerous previous studies indicated that TiO_2 doping with a noble metal can effectively increase absorption and significantly enhance the visible light photocatalytic properties of TiO_2 [35].

3.6. Photocatalytic Activity and Recycled Photocatalytic Degradation Performance. The photocatalytic activities of TiO_2, TiO_2-T, TiO_2/Pd, and TiO_2/PdO were evaluated in terms of the decolorization of Rh B under visible light irradiation as shown in Figure 6(a). The photocatalytic performances of a blank Rh B solution without photocatalysts and TiO_2/PdO without visible light irradiation are also included in Figure 6(a) for comparison. The chart clearly shows that the photocatalytic degradation rate of Rh B increased with the intensity of irradiation and the relative photocatalytic activity of the catalysts decreased in the order TiO_2/PdO>TiO_2/Pd>TiO_2-T>TiO_2>Bare>TiO_2/PdO (black) (Table 3). First, the final photocatalytic degradation rate of Rh B during self-degradation and adsorption was lower than that under visible light and with the presence of photocatalysts, thereby revealing the photocatalytic activity of these samples. Second, TiO_2/PdO and TiO_2/Pd exhibited higher activities than TiO_2 and TiO_2-T. The higher activities of TiO_2/PdO and TiO_2/Pd could be explained in terms of the enhancement of UV-Vis absorbance spectra due to Pd and PdO doping (as shown in Figure 5) [35]. The enhancement of UV-Vis absorbance spectra of the doped samples represents their optical absorption property, offering a higher photocatalytic activity. Third, the visible light photocatalytic activities of TiO_2/PdO and TiO_2-T after calcination were higher than those before calcination (TiO_2 and TiO_2/Pd). This finding could be ascribed to the crystallinity of the samples; that is, high crystallinity indicates few defects, which could lead to the slowed recombination of photogenerated hole-electron pairs [36]. The crystallinity of TiO_2-T and TiO_2/PdO was improved by calcination (as shown in Figure 1). Thus, the photocatalytic activities of TiO_2/PdO and TiO_2-T were better than those of TiO_2 and TiO_2/Pd.

Table 3: Photocatalytic degradation activity for TiO_2, TiO_2-T, TiO_2/Pd, and TiO_2/PdO and previously reported photocatalysts for Rh B degradation under visible light irradiation.

Sample	Degradation (%)	First-order kinetic equation	k (min^{-1})
Bare	28.6	$-\ln(C/C_0) = 0.0079t$	0.0079
TiO_2/PdO (black)	3.4	$-\ln(C/C_0) = 0.00026t$	0.00026
TiO_2	76.23	$-\ln(C/C_0) = 0.034t$	0.034
TiO_2-T	89.14	$-\ln(C/C_0) = 0.058t$	0.058
TiO_2/Pd	94.04	$-\ln(C/C_0) = 0.063t$	0.063
TiO_2/PdO	100	$-\ln(C/C_0) = 0.126t$	0.126
Pd/TiO_2 [a] [27]	94	—	—
PdO/TiO_2 [b] [27]	94	—	—
TiO_2 [c] [12]	85	$-\ln(C/C_0) = 0.013t$	0.013
P25 [d] [11]	—	$-\ln(C/C_0) = 0.023t$	0.023

Footnotes: The test conditions for [a], [b], [c], and [d] in the reference are 30 mg of the photocatalysts and 50 mL of a solution of Rh B (10 mg/L, irradiation time is 50 min), 30 mg of photocatalysts and 50 mL of a solution of Rh B (10 mg/L, irradiation time is 150 min), and 30 mg of photocatalysts and 50 mL of a solution of Rh B (4.8 mg/L, irradiation time is 120 min), respectively.

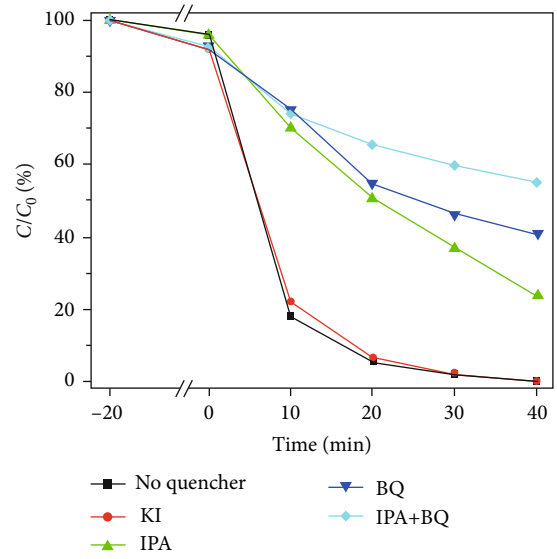

Figure 7: Effect of different scavengers on the degradation of Rh B by the TiO_2/PdO photocatalysts.

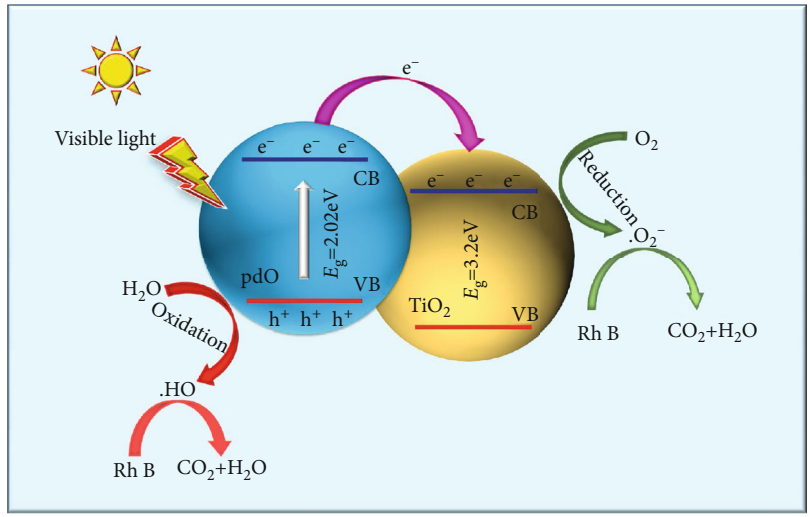

FIGURE 8: Photocatalytic mechanism of TiO_2/PdO photocatalysts under visible light irradiation.

The UV-Vis spectra changes in the dye solution over various time intervals are shown in Figure 6(b) to understand and clarify the changes in the molecular structure of Rh B in the presence of TiO_2/PdO under visible light irradiation. The absorption peak of 550 nm continuously descended with increasing exposure time and almost vanished after 40 min of irradiation. This result is consistent with the gradual color change of the reaction solution from peach to almost colorless during the different reaction times, which suggests that TiO_2/PdO exhibited an excellent photocatalytic activity for Rh B degradation. In addition, most dye degradation processes occurred in the initial minutes. Immediately after 10 min, TiO_2/PdO obtained a degradation percentage of 81.7%. Therefore, the degradation rate for TiO_2/PdO in the initial minutes was high.

The kinetics of the photodegradation of Rh B in the presence of TiO_2, TiO_2-T, TiO_2/Pd, and TiO_2/PdO was also studied. The $-\ln(C/C_0)$ of these samples presented a good linear reaction with irradiation time (shown in Figure 6(c)), which means that the photodegradation of Rh B follows the rules of the first-order reaction kinetics $-\ln(C/C_0) = kt$, where k is the first-order rate constant, and C_0 and C are the concentrations of Rh B at irradiation times 0 and t, respectively [11]. The calculated kinetic rate constants are summarized in Table 3. TiO_2/PdO had a maximum k value of 0.126 min^{-1}, whereas the others had 0.034 min^{-1} (TiO_2), 0.058 min^{-1} (TiO_2-T), 0.063 min^{-1} (TiO_2/Pd), 0.0079 min^{-1} (Bare), and 0.00026 min^{-1} (TiO_2/PdO black). Moreover, the rate constant coincides with the final degradation rate (Table 3) of the photocatalytic degradation in Figure 6(a).

The degradation (%) and rate constant (k) of previously reported photocatalysts, such as Pd/TiO_2 [27], PdO/TiO_2 [27], TiO_2 [12], and P25 [11], are listed in Table 3 for comparison. Notably, the degradation and rate constant of TiO_2/PdO were determined to be 100% and 0.126 min^{-1}, which were much larger than those of PdO/TiO_2 and other photocatalysts. The high degradation and rate constant of TiO_2/PdO could be attributed to its wide range of optical absorption, high crystallinity, and large pore size.

Recycling of catalysts is a key step in assessing the practical application of photocatalysts. To confirm the possibility of recycling the obtained photocatalysts, four recycling experiments were performed with a TiO_2/PdO sample in the photocatalytic degradation of Rh B. As shown in Figure 6(d), the degradation rates of four recycling instances reached up to 99.8%, 99.0%, 98.4%, and 96.6%. The results reveal that the separation of photocatalysts was effective. Thus, the photocatalyst is basically stable and therefore promising for environmental remediation.

3.7. Active Species and Mechanism Underlying the Photocatalytic Degradation of Rh B. The effect of different scavengers on the degradation of Rh B by the TiO_2/PdO was investigated to confirm the main active species and provide insight into the potential photocatalytic mechanism of TiO_2/PdO photocatalysts. Three different scavengers, namely, BQ (a $\cdot O_2^-$ radical scavenger), IPA (a ·OH radical scavenger), and KI (h^+ scavenger), were introduced into the reaction systems [37, 38]. Figure 7 shows that BQ markedly suppressed the degradation rate of Rh B, whereas the presence of KI barely inhibits the photocatalytic efficiency. Compared with KI, IPA hindered the degradation of Rh B. Thus, we conducted a set of comparative experiments. Both BQ and IPA scavengers were added to the same set of experiments to obtain the results shown in Figure 7. IPA+BQ inhibited the degradation of Rh B more strongly than BQ. Therefore, these results suggest that ·OH and $\cdot O_2^-$ were the primary active species that governed the photocatalytic process, and h^+ was not the main active species in the degradation of Rh B by the TiO_2/PdO.

On the basis of the above investigation and analysis, we propose the possible mechanism for the charge transfer and separation processes underlying the photocatalytic degradation of TiO_2/PdO as schematically illustrated in Figure 8. Upon visible light irradiation, PdO absorbs incident photons and generates electron-hole pairs:

$$\mathrm{PdO} + \mathrm{hv} \longrightarrow e_{\mathrm{CB}}^- + \mathrm{h}_{\mathrm{VB}}^+, \quad (1)$$

where e^-_{CB} and h^+_{VB} are the electrons in the conduction band (CB) and the holes in the valence band (VB), respectively. The photogenerated electrons transfer from the CB of PdO to the CB of TiO_2, while the photogenerated holes remain in the VB of PdO. Thus, the electrons and holes can be effectively separated to inhibit their recombination [39]. Finally, the electrons reduce O_2 to $\cdot O_2^-$ radicals; the holes can react easily with the surface-bound H_2O and generate ·OH radicals. The powerful oxidizing agent ($\cdot O_2^-$ and ·OH) can then react with the organic dyes and produce CO_2, H_2O, and so on [12].

$$e^-_{CB} + O_2 \longrightarrow \bullet O_2^-, \text{dye} + \bullet O_2^- \longrightarrow H_2O + CO_2,$$
$$h^+_{VB} + H_2O \longrightarrow \bullet OH + H^+, \text{dye} + \bullet OH \longrightarrow H_2O + CO_2. \quad (2)$$

4. Conclusion

We have successfully synthesized TiO_2/Pd and TiO_2/PdO hollow spheres. The photocatalysis efficiencies of all as-prepared samples were evaluated through the photocatalytic degradation of Rh B under visible light irradiation. The results indicated that TiO_2/PdO demonstrated a higher photocatalytic activity than the other samples, and a Rh B of 30 mg/L could be completely (100%) degraded by TiO_2/PdO under visible light irradiation within 40 min. This result can be ascribed to the wide-range optical absorption, high crystallinity, and large pore size of TiO_2/PdO. In addition, TiO_2/PdO can be easily separated and retain its photocatalytic efficiency for at least four cycles of reaction under visible light irradiation. Thus, TiO_2/PdO is a promising photocatalyst for the decomposition of recalcitrant and emerging pollutants in water and wastewater treatments.

Data Availability

The data used to support the findings of this study are available from the corresponding author upon request.

Conflicts of Interest

The authors declare that they have no conflict of interest.

Acknowledgments

We are grateful for the financial support from the National Natural Science Foundation of China (project no. 51327804) and Open Project of State Key Laboratory Cultivation Base for Nonmetal Composites and Functional Materials (project no. 14tdfk05).

References

[1] G. Liu, L. Wang, H. G. Yang, H. M. Cheng, and G. Q. (Max) Lu, "Titania-based photocatalysts-crystal growth, doping and heterostructuring," *Journal of Materials Chemistry*, vol. 20, no. 5, pp. 831–843, 2010.

[2] M. Montazer, E. Pakdel, and A. Behzadnia, "Novel feature of nano-titanium dioxide on textiles: antifelting and antibacterial wool," *Journal of Applied Polymer Science*, vol. 121, no. 6, pp. 3407–3413, 2011.

[3] Y. J. Kim, M. H. Lee, H. J. Kim et al., "Formation of highly efficient dye-sensitized solar cells by hierarchical pore generation with nanoporous TiO_2 Spheres," *Advanced Materials*, vol. 21, no. 36, pp. 3668–3673, 2009.

[4] X. P. Zhao and J. B. Yin, "Preparation and electrorheological characteristics of rare-earth-doped TiO_2 Suspensions," *Chemistry of Materials*, vol. 14, no. 5, pp. 2258–2263, 2002.

[5] B. X. Wang and X. P. Zhao, "Wettability of bionic nanopapilla particles and their high electrorheological activity," *Advanced Functional Materials*, vol. 15, no. 11, pp. 1815–1820, 2005.

[6] J. Thiel, L. Pakstis, S. Buzby et al., "Antibacterial properties of silver-doped titania," *Small*, vol. 3, no. 5, pp. 799–803, 2007.

[7] S. M. Gupta and M. Tripathi, "A review of TiO_2 nanoparticles," *Chinese Science Bulletin*, vol. 56, no. 16, pp. 1639–1657, 2011.

[8] M. Dahl, Y. Liu, and Y. Yin, "Composite titanium dioxide nanomaterials," *Chemical Reviews*, vol. 114, no. 19, pp. 9853–9889, 2014.

[9] X. Xia, J. Shen, F. Cao et al., "A facile synthesis of hydroxyapatite for effective removal strontium ion," *Journal of Hazardous Materials*, vol. 368, pp. 326–335, 2019.

[10] L. Xiang, X. Zhao, J. Yin, and B. Fan, "Well-organized 3D urchin-like hierarchical TiO_2 microspheres with high photocatalytic activity," *Journal of Materials Science*, vol. 47, no. 3, pp. 1436–1445, 2012.

[11] L. L. Lai and J. M. Wu, "A facile synthesis of hierarchical TiO_2 for dye adsorption and photocatalysis," *RSC Advances*, vol. 4, no. 68, pp. 36212–36217, 2014.

[12] D. Sarkar and K. K. Chattopadhyay, "Facile synthesis of large scale mesoporous TiO_2microspheres by template-free hydrothermal process: their photocatalysis degradation," in *16th International Workshop on Physics of Semiconductor Devices*, vol. 8549, Kanpur, India, October 2012no. 16, Article ID 854927.

[13] K. Prabakar, T. Takahashi, T. Nezuka et al., "Visible light-active nitrogen-doped TiO_2 thin films prepared by DC magnetron sputtering used as a photocatalyst," *Renewable Energy*, vol. 33, no. 2, pp. 277–281, 2008.

[14] R. M. Mohamed and E. S. Baeissa, "Mordenite encapsulated with Pt–TiO_2: Characterization and applications for photocatalytic degradation of direct blue dye," *Journal of Alloys and Compounds*, vol. 558, pp. 68–72, 2013.

[15] R. M. Mohamed, "UV-assisted photocatalytic synthesis of TiO_2-reduced graphene oxide with enhanced photocatalytic activity in decomposition of sarin in gas phase," *Desalination and Water Treatment*, vol. 50, no. 1-3, pp. 147–156, 2012.

[16] W. Shu, Y. Liu, Z. Peng, K. Chen, C. Zhang, and W. Chen, "Synthesis and photovoltaic performance of reduced graphene oxide–TiO_2 nanoparticles composites by solvothermal method," *Journal of Alloys and Compounds*, vol. 563, pp. 229–233, 2013.

[17] C. Di Valentin, E. Finazzi, G. Pacchioni et al., "Density functional theory and electron paramagnetic resonance study on the effect of N-F codoping of TiO_2," *Chemistry of Materials*, vol. 20, no. 11, pp. 3706–3714, 2008.

[18] Y. Cao, Z. Zhao, J. Yi et al., "Luminescence properties of Sm^{3+}-doped TiO_2 nanoparticles: synthesis, characterization, and mechanism," *Journal of Alloys and Compounds*, vol. 554, pp. 12–20, 2013.

[19] R. M. Mohamed and E. S. Aazam, "H_2 production with low CO selectivity from photocatalytic reforming of glucose on Ni/TiO_2-SiO_2," *Chinese Journal of Catalysis*, vol. 33, no. 2-3, pp. 247–253, 2012.

[20] R. M. Mohamed and E. S. Aazam, "Preparation and characterization of platinum doped porous titania nanoparticles for photocatalytic oxidation of carbon monoxide," *Journal of Alloys and Compounds*, vol. 509, no. 41, pp. 10132–10138, 2011.

[21] R. M. Mohamed and E. S. Aazam, "Characterization and Catalytic Properties of Nano-Sized Au Metal Catalyst on Titanium Containing High Mesoporous Silica (Ti-HMS) Synthesized by Photo- Assisted Deposition and Impregnation Methods," *International Journal of Photoenergy*, vol. 2011, Article ID 137328, 7 pages, 2011.

[22] R. M. Mohamed and I. A. Mkhalid, "Characterization and catalytic properties of nano-sized Ag metal catalyst on TiO_2–SiO_2 synthesized by photo-assisted deposition and impregnation methods," *Journal of Alloys and Compounds*, vol. 501, no. 2, pp. 301–306, 2010.

[23] N. Castillo, R. Pérez, M. J. Martínez-Ortiz, L. Díaz-Barriga, L. García, and A. Conde-Gallardo, "Structural analysis of platinum–palladium nanoparticles dispersed on titanium dioxide to evaluate cyclo-olefines reactivity," *Journal of Alloys and Compounds*, vol. 495, no. 2, pp. 453–457, 2010.

[24] M. Y. Abdelaal and R. M. Mohamed, "Novel Pd/TiO_2 nanocomposite prepared by modified sol–gel method for photocatalytic degradation of methylene blue dye under visible light irradiation," *Journal of Alloys and Compounds*, vol. 576, pp. 201–207, 2013.

[25] X. Li, B. Jin, J. Huang, Q. Zhang, R. Peng, and S. Chu, "$Fe_2O_3/ZnO/ZnFe_2O_4$ composites for the efficient photocatalytic degradation of organic dyes under visible light," *Solid State Sciences*, vol. 80, pp. 6–14, 2018.

[26] X. Li, J. Xiong, Y. Xu, Z. Feng, and J. Huang, "Defect-assisted surface modification enhances the visible light photocatalytic performance of g-C_3N_4@C-TiO_2 direct Z-scheme heterojunctions," *Chinese Journal of Catalysis*, vol. 40, no. 3, pp. 424–433, 2019.

[27] H. Khojasteh, M. Salavati-Niasari, A. Abbasi, F. Azizi, and M. Enhessari, "Synthesis, characterization and photocatalytic activity of PdO/TiO_2 and Pd/TiO_2 nanocomposites," *Journal of Materials Science: Materials in Electronics*, vol. 27, no. 2, pp. 1261–1269, 2016.

[28] C. J. Huang, F. M. Pan, and I. C. Chang, "Enhanced photocatalytic decomposition of methylene blue by the heterostructure of PdO nanoflakes and TiO_2 nanoparticles," *Applied Surface Science*, vol. 263, pp. 345–351, 2012.

[29] J. Xiong, X. Li, J. Huang et al., "CN/rGO@BPQDs high-low junctions with stretching spatial charge separation ability for photocatalytic degradation and H_2O_2 production," *Applied Catalysis B: Environmental*, vol. 266, article 118602, 2020.

[30] D. Li, Q. Qin, X. Duan, J. Yang, W. Guo, and W. Zheng, "General one-pot template-free hydrothermal method to metal oxide hollow spheres and their photocatalytic activities and lithium storage properties," *ACS Applied Materials & Interfaces*, vol. 5, no. 18, pp. 9095–9100, 2013.

[31] J. Shen, G. Ma, J. Zhang, W. Quan, and L. Li, "Facile fabrication of magnetic reduced graphene oxide-$ZnFe_2O_4$ composites with enhanced adsorption and photocatalytic activity," *Applied Surface Science*, vol. 359, pp. 455–468, 2015.

[32] Y. Xu, D. Sun, H. Hao, D. Gao, and Y. Sun, "Non-stoichiometric Co (II), Ni (II), Zn (II)-ferrite nanospheres: size controllable synthesis, excellent gas-sensing and magnetic properties," *RSC Advances*, vol. 6, no. 101, pp. 98994–99002, 2016.

[33] Z. W. Ding, S. Chen, Z. Q. Liu, C. F. Jiang, and W. Chu, "Mesoporous sulfur-doped TiO_2 microspheres for catalytic degradation of methylene blue under visible light," *Advanced Materials Research*, vol. 1118, pp. 242–250, 2015.

[34] J. P. Liu, H. Zhao, X. L. Song, and X. L. Li, "Effects of calcination temperature on structure of titanium oxide photocatalyst," *Inorganic Chemicals Industry*, vol. 41, no. 9, pp. 37–39, 2009.

[35] X. Liu, Y. Sun, Y. Wang, L. Zhang, and J. Lu, "Synthesis and photocatalytic activities of Nd-doped TiO_2 mesoporous microspheres," *Functional Materials Letters*, vol. 9, no. 1, article 1650013, 2016.

[36] Z. Li, Z. Ren, Y. Qu et al., "Hierarchical N-doped TiO_2 Microspheres with exposed (001) facets for enhanced visible light catalysis," *European Journal of Inorganic Chemistry*, vol. 2014, no. 12, pp. 2146–2152, 2014.

[37] S. Wang, C. Liu, K. Dai et al., "Fullerene C_{70}–TiO_2 hybrids with enhanced photocatalytic activity under visible light irradiation," *Journal of Materials Chemistry A*, vol. 3, no. 42, pp. 21090–21098, 2015.

[38] X. Zhang, Q. Wang, L. H. Zou, and J. W. You, "Facile fabrication of titanium dioxide/fullerene nanocomposite and its enhanced visible photocatalytic activity," *Journal of Colloid and Interface Science*, vol. 466, pp. 56–61, 2016.

[39] X. Liu, Y. Li, J. Yang et al., "Enhanced photocatalytic activity of CdS-decorated TiO_2/carbon core-shell microspheres derived from microcrystalline cellulose," *Materials*, vol. 9, no. 4, p. 245, 2016.